ACS NANO

www.acsnano.org

ARTICLE

Coexisting Ferromagnetic–Antiferromagnetic State and Giant Anomalous Hall Effect in Chemical Vapor Deposition-Grown 2D Cr_5Te_8

Lei Fu,* A. E. Llacsahuanga Allcca, and Yong P. Chen*

Cite This: *ACS Nano* 2024, 18, 33381–33389

Read Online

ACCESS | Metrics & More | Article Recommendations | Supporting Information

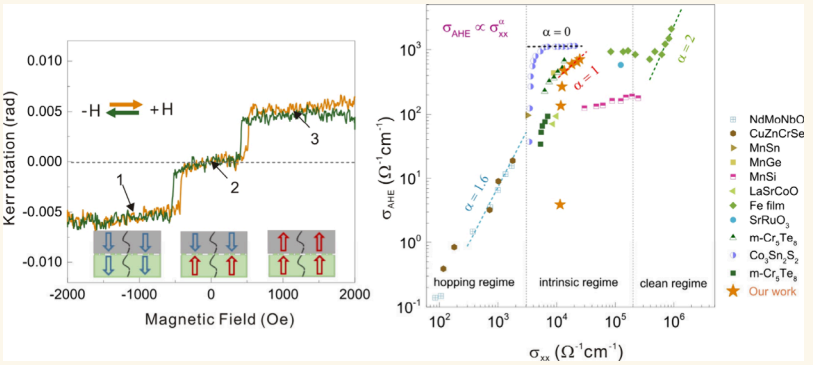

ABSTRACT: **Two-dimensional (2D) magnets, as an important member of the 2D material family, have emerged as a promising platform for spintronic devices. Herein, we report the chemical vapor deposition (CVD) growth of highly crystalline submillimeter-scale self-intercalated metallic 2D ferromagnetic (FM) trigonal chromium telluride (Cr_5Te_8) flakes on inert mica substrates. Through magneto-optical and magnetotransport measurements, we unveil the exceptional magnetic properties of these 2D flakes. The trigonal Cr_5Te_8 flakes exhibit a strong anisotropic FM order with a Curie temperature above 220 K. Notably, an emergent antiferromagnetic (AFM) state is observed in the MOKE signal from ultrathin Cr_5Te_8 flakes around the Curie temperature. The AFM state has a relatively weak interlayer exchange coupling, allowing a switching between the interlayer AFM and FM states by tuning the temperature. Meanwhile, the trigonal Cr_5Te_8 flakes exhibit a giant anomalous Hall effect (AHE), with an anomalous Hall conductivity of 710 Ω^{-1} cm^{-1} and an anomalous Hall angle of 3.5% at zero magnetic field, surpassing typical itinerant ferromagnets. Further analysis suggests that the AHE in trigonal Cr_5Te_8 is primarily driven by the skew-scattering mechanism rather than the intrinsic or extrinsic side-jump mechanism. These findings demonstrate the potential of CVD-grown ultrathin Cr_5Te_8 flakes as a promising 2D magnetic material with exceptional AHE properties for future spintronic applications.**

KEYWORDS: *two-dimensional magnets, chemical vapor deposition, coexisting ferromagnetic–antiferromagnetic state, giant anomalous Hall effect, chromium telluride*

INTRODUCTION

The exploration of two-dimensional (2D) materials has provided possibilities in the field of semiconductors,[1−3] superconductivity,[4] ferroelectricity,[5] magnetism,[6] and others,[7,8] offering potential opportunities for the development of electronic and spintronic devices. Among such diverse 2D materials, 2D ferromagnets can have long-range ferromagnetic (FM) order even at the one atom-thick level,[6,9−12] deepening our understanding of FM behavior and expanding their applications in spintronic devices and high-density data storage. Recently, some works have documented the intrinsic long-range FM ordering in atomic-thick (few-layer) metallic Fe_3GeTe_2,[9−12] VSe_2,[13] $CrTe_2$,[14] and $Cr_{1/3}CrTe_2$,[15] as well as insulating $Cr_2Ge_2Te_6$[16] and CrI_3,[6,17] initiating fundamental research in 2D ferromagnetism.

Received: June 29, 2024
Revised: November 6, 2024
Accepted: November 19, 2024
Published: November 27, 2024

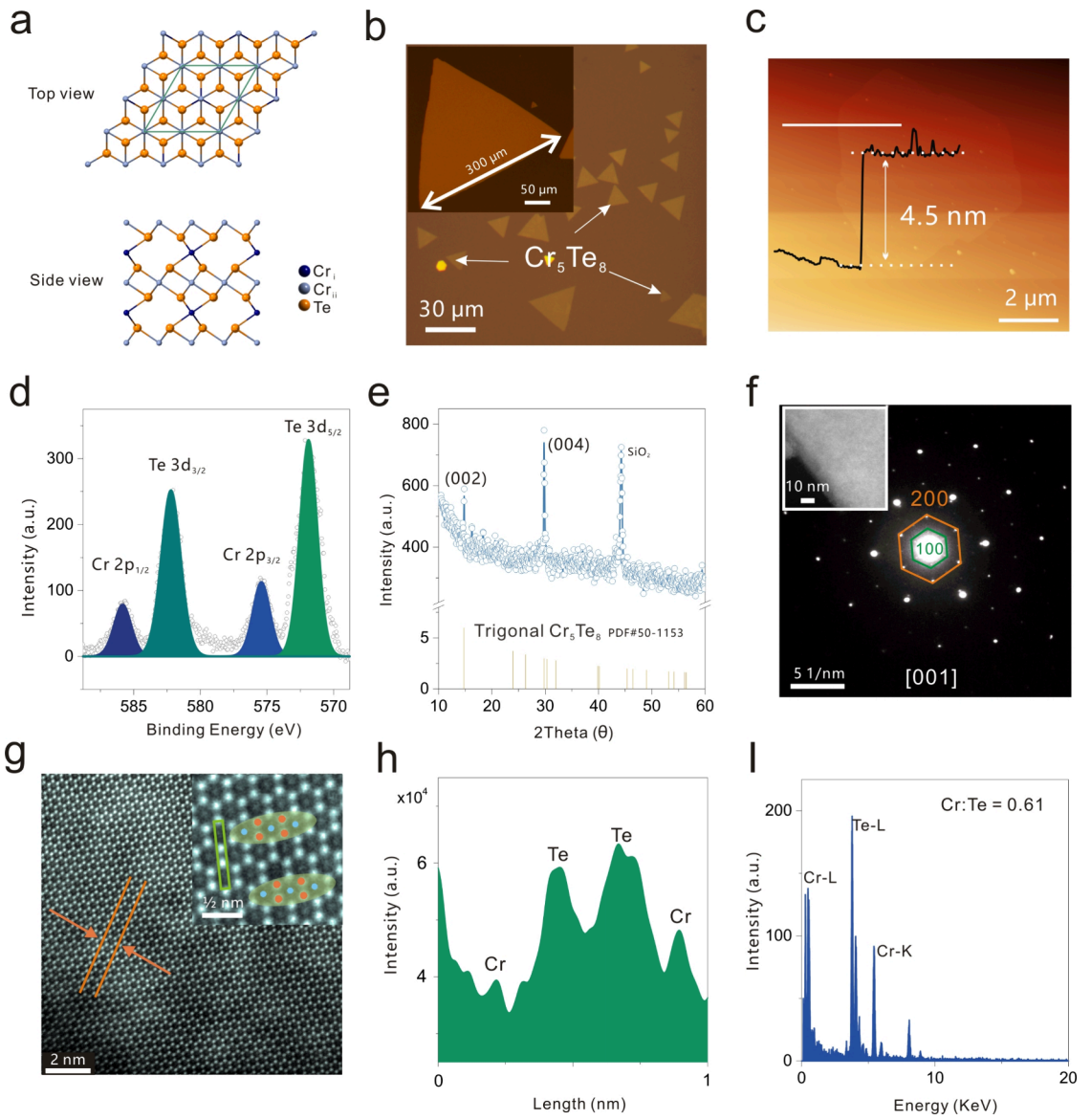

Figure 1. Synthesis and atomic structure of Cr_5Te_8 flakes grown by a sublimed salt-assisted ambient pressure CVD method on mica substrates. (a) Crystal structure of Cr_5Te_8. (b) Optical microscopy image of the Cr_5Te_8 flakes on mica. Scale bar, 30 μm. Inset: Cr_5Te_8 flake with lateral dimensions up to 300 μm. Scale bar, 50 μm. (c) Representative atomic force microscopy image from a 4.5 nm-thick Cr_5Te_8 flake, with the corresponding cross-sectional height profile along the white line. Scale bar, 2 μm. (d, e) XPS spectrum and XRD pattern of the Cr_5Te_8 flakes transferred on SiO_2/Si substrates. (f) SAED pattern of a Cr_5Te_8 flake transferred on a TEM grid. Inset: STEM image of the edge of the Cr_5Te_8 flake. (g) Atomic-resolution HAADF-STEM image of a typical Cr_5Te_8 flake along the [001] direction. Orange lines and arrows demarcate the (100) lattice spacing (0.68 nm). Inset: zoomed-in image showing Te (brighter) and Cr (dimmer) atoms, some false-colored as orange and blue, respectively. (h) Intensity line profile along the green boxline in the inset of (g). (i) EDS elemental analysis of the Cr_5Te_8 flake.

Self-intercalated layered chromium chalcogenides consisting of alternating stacks of Cr-intercalary and Cr-full layers along the *c*-direction, such as $CrTe_2$,[14] $Cr_{1/3}CrTe_2$,[15] and Cr_5Te_8,[18−23] have attracted strong interest recently due to their phases and intriguing magnetic properties. van der Waals (vdW) FM 1T-phase $CrTe_2$ layers crystallize in the CdI_2-type structure with the AA stacking order.[14] In the growth process, a portion of the chromium atoms will intercalate into $CrTe_2$ layers, regarded as $Cr_{1+x}Te_2$ ($x \approx 0-0.33$).[24−27] Previous reports have demonstrated that $Cr_{1/3}CrTe_2$ is a magnetic metal with a high Curie temperature (T_c) over 200 K and distinct magnetocrystalline anisotropy.[15,24−27] Notably, Cr_5Te_8 with its geometrically frustrated structure is predicted to give rise to nontrivial magnetic structures and rich transport properties, such as the topological Hall effect and a large anomalous Hall effect (AHE).[18] Robust 2D ferromagnetism with a T_c exceeding 400 K was observed in $Cr_5Te_8/CrTe_2$ heterostructures.[23] Two distinct types of magnetic domains, magnetic bubbles and thickness-dependent maze-like magnetic domains, are observed in Cr_5Te_8 nanosheets.[19] By means of self-doping, Cr_5Te_8 has been reported with the emergence of an interesting antiferromagnetic (AFM) ordering and a significant giant magnetoresistance effect.[22] The relatively weak interlayer exchange coupling in the AFM state also allows for field-induced switching between the AFM and FM states. Temperature tuning primarily affects the interlayer exchange

https://doi.org/10.1021/acsnano.4c08700
ACS Nano 2024, 18, 33381−33389

coupling through thermal expansion/contraction of the lattice, while field-induced switching directly overcomes the coupling energy with an external magnetic field. Moreover, a colossal anomalous Hall effect in a distorted monoclinic Cr_5Te_8 phase has been documented, showcasing an anomalous Hall conductivity of 650 Ω^{-1} cm^{-1} and an anomalous Hall angle of 5%.[21] This significant AHE is particularly valuable for the development of energy efficient spintronic devices with low Joule heating. Consequently, Cr_5Te_8 emerges as a promising candidate among self-intercalated chromium chalcogenide compounds due to its intriguing magnetism and transport properties, making it ripe for further exploration in technological applications.

Herein, we realize the chemical vapor deposition (CVD) growth of submillimeter-scale 2D self-intercalated Cr_5Te_8 flakes via vdW epitaxy on mica substrates. Importantly, our samples exhibit strong anisotropic FM order, and a T_c above 220 K can be retained down to few-layer atomic thickness. Notably, an emergent AFM state is observed in the magneto-optical Kerr effect (MOKE) signal from the ultrathin Cr_5Te_8 flakes in the temperature window of 160−180 K. The AFM state has a relatively weak interlayer exchange coupling, allowing a switching between the interlayer AFM and FM states by tuning the temperature. Moreover, through comprehensive magneto-optical and magnetotransport measurements, we unveil the exceptional AHE properties of these 2D FM Cr_5Te_8 flakes, including a giant anomalous Hall conductivity of 710 Ω^{-1} cm^{-1} and an anomalous Hall angle of 3.5% at zero magnetic field, surpassing those of typical itinerant ferromagnets. Further analysis suggests that the anomalous Hall effect in trigonal Cr_5Te_8 is primarily driven by the skew-scattering mechanism, rather than the intrinsic or extrinsic side-jump mechanism. Our research will contribute to the controlled CVD synthesis of 2D magnetic materials and thereby outline a route toward constructing next-generation spintronic devices.

RESULTS AND DISCUSSION

The CVD method has been adopted to grow multiple transition metal dichalcogenide (TMDC) compounds.[14,15,19−23,28] Nevertheless, the CVD growth of atomically thin tellurides remains challenging due to the low chemical reactivity of Te powder,[15,20] such as low sublimation rates, inefficient transport, and slow nucleation rates. In order to realize self-intercalated Cr_5Te_8 flakes with atomic thickness and high crystallinity, we have adopted a medium-assisted strategy for epitaxial growth, which can maintain the continuous evaporation of metal precursors in the whole growth process. In our case, the metal precursor is Cr powder, and sodium chloride (NaCl) is used as the auxiliary evaporation medium (Figure S1). It is worth mentioning that previous works have reported that NaCl, with its suitable melting point, can reduce the energy barrier and increase the crystal growth rate.[28] In the growth process, the mixed carrier gas of hydrogen and argon is utilized to help the crystals grow rapidly when the temperature is raised to 800 °C.

Figure 1a exhibits the crystal structure of Cr_5Te_8, accounting for a portion of the chromium atoms (Cr_i) being intercalated into the $CrTe_2$ layers. Here, Cr_5Te_8 belongs to the $P\bar{3}m1$ space group with the trigonal phase. The interlayer and intralayer chromium atoms are identified as Cr_i and Cr_{ii}, respectively, distinguished by dark blue and light blue colors. The uniformly intercalating Cr_i atoms have a 50% linear filling rate compared to the Cr_{ii} atoms in the $CrTe_2$ layers, forming a 2 × 2 supercell of $CrTe_2$, doubling the lattice constant.[20−23] The identification of the atomic structure is detailed later. In our work, freshly cleaved mica due to its inert nature with no dangling bonds was used as the substrate for Cr_5Te_8 epitaxial growth. Figure 1b displays an optical microscopy image of atomically thin Cr_5Te_8 flakes (mostly triangular-shaped) grown on a mica substrate, and the largest lateral size can be up to 300 μm (Figure 1b, inset). Since it is a quasi-two-dimensional crystal, chromium atoms will intercalate into the gaps, leading to an increase in its thickness as it grows larger. Atomic force microscopy images presented a typical flake thickness of 4.5 nm (extracted from the step height along the white dotted line in Figure 1c). X-ray photoelectron spectroscopy (XPS) characterization was employed to explore the composition and valence of elements. As shown in Figure 1d, the peaks located at binding energies of 575.3 and 585.9 eV are ascribed to the Cr $2p_{3/2}$ and Cr $2p_{1/2}$ states, and the peaks located at 572.1 and 582.3 eV are attributed to the Te $3d_{5/2}$ and Te $3d_{3/2}$ states, indicating a $Cr^{3.2+}$ state and a Te^{2-} state, respectively.[19−21] X-ray diffraction (XRD) was utilized to elucidate the crystal structure. As indicated in Figure 1e, the XRD peaks indicate a single-crystal pattern, corresponding well to the (002) and (004) crystal planes of the trigonal structured Cr_5Te_8 from PDF#50-1153.[19−21]

To further confirm the crystal structure of the grown flakes, high-angle annular dark-field scanning transmission electron microscopy (HAADF-STEM) was employed to characterize the grown flakes placed onto a holey carbon TEM grid. Our results are consistent with previous STEM measurements,[20−23] indicating the separation between the interlayer Cr_i atoms is twice that compared to the intralayer Cr_{ii} atoms, forming a 2 × 2 supercell of $CrTe_2$. This arrangement manifests in the {200} and {100} crystal plane families (depicted by orange and green hexagons), illustrated in the selected area electron diffraction (SAED) pattern from the [001] zone axis of a Cr_5Te_8 flake in Figure 1f, with the brightest {200} spot originating from the $CrTe_2$ backbone, while the inner {100} supercell spots arisie from ordered Cr_i atoms between $CrTe_2$ layers. The ordered arrangement of Cr_i atoms gives another periodicity in reciprocal space, with the same orientation but half the frequency of the $CrTe_2$ lattice. This observation aligns with the XRD structural analysis, providing insights into the unique atomic arrangement of the trigonal Cr_5Te_8 phase. Through a high-resolution Z-contrast STEM image, we directly distinguished the Cr (dark) and Te (bright) atoms with the (100) plane lattice spacing at 0.68 nm, as indicated in Figure 1g. According to the intensity distribution along the green boxline in the inset of Figure 1g, the Cr−Cr distance of Cr_5Te_8 was measured to be 0.70 nm, corresponding to the alternating bright (Cr_{ii} on Cr_i) and dim (Cr_{ii}) contrast of adjacent Cr columns, consistent with the intercalated Cr_i atoms having double the periodicity of Cr_i (Figure 1h). Energy dispersive X-ray spectroscopy (EDS) analysis of our sample (Figure 1i) exhibits that our sample contains Cr and Te elements with the ratio of ∼0.61, in good agreement with the atomic ratio of ∼5:8.[20−23] The elemental mapping images illustrate that the Cr and Te elements are evenly distributed across the selected area (Figure S2). The XRD pattern, in-plane STEM Z-contrast image, and SAED and EDS analyses provide a means to identify the chemical composition and trigonal phase of the as-synthesized Cr_5Te_8.

https://doi.org/10.1021/acsnano.4c08700
ACS Nano 2024, 18, 33381−33389

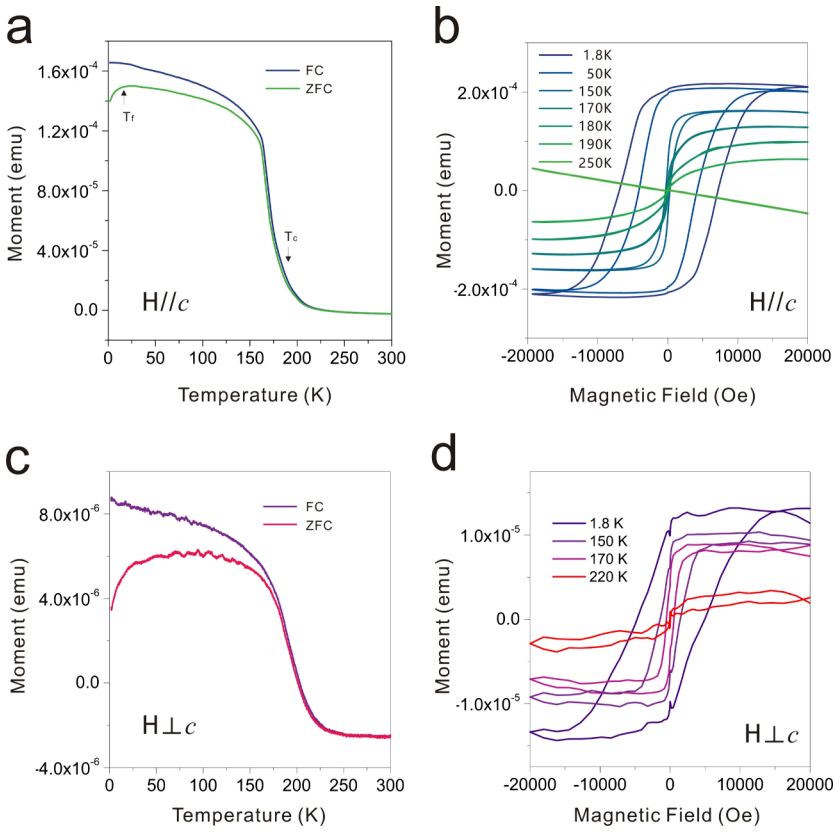

Figure 2. Magnetic properties of Cr_5Te_8 samples on SiO_2/Si substrates. (a, c) Temperature-dependent magnetic susceptibility measured at a field 0.1 T for out-of-plane (H//c) and in-plane (H⊥c), respectively. T_f is the freezing temperature, defined as the temperature where the susceptibility shows a drop in the ZFC curve. T_c is the Curie temperature, at which the cooling sample undergoes a phase transition from a paramagnetic state to a ferromagnetic state. (b, d) Magnetic field-dependent susceptibility (characterizing hysteresis loops) measured from −2 to 2 T obtained at different temperatures for out-of-plane and in plane applied fields, respectively.

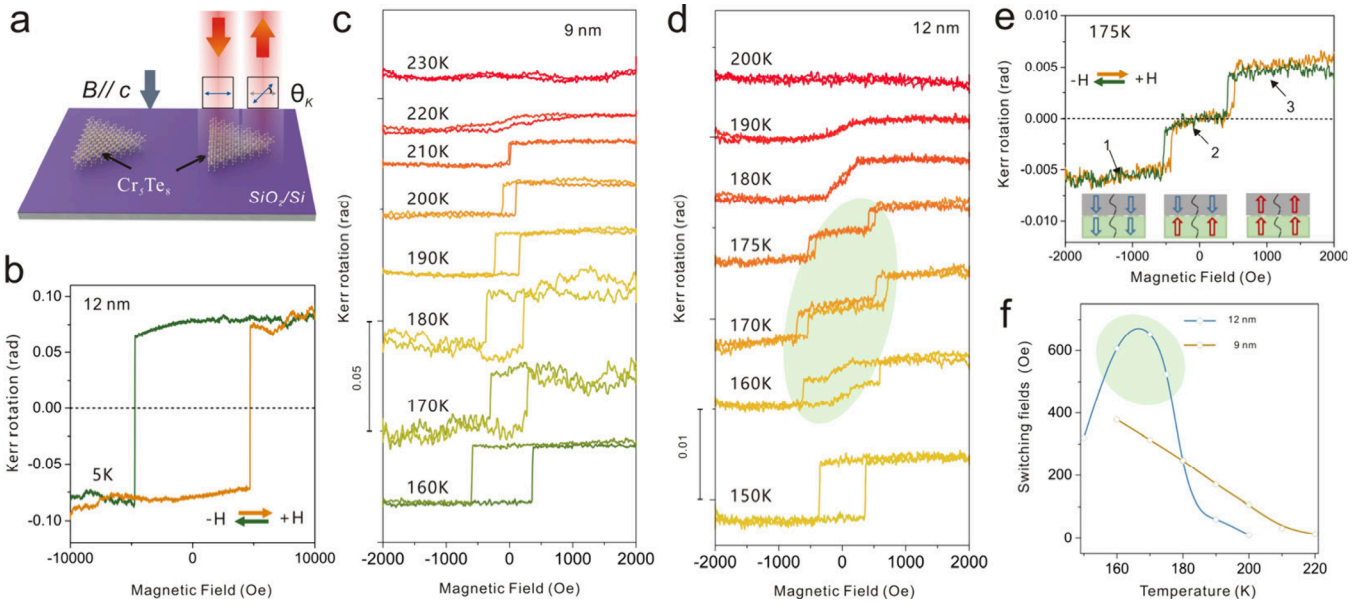

Figure 3. Coexisting antiferromagnetic−ferromagnetic states of individual Cr_5Te_8 flakes revealed in MOKE measurements. (a) The schematic of the MOKE measurement of the Cr_5Te_8 flake. (b) Polar MOKE signal of a 12 nm-thick Cr_5Te_8 flake at 5 K. (c, d) MOKE curves (offset for clarity) measured at different temperature for two flakes with thicknesses of 9 and 12 nm, respectively. The 12 nm-thick flake shows coexisting antiferromagnetic−ferromagnetic states. T_c was extracted from the plots of the temperature-dependent MOKE signal at zero field. (e) The MOKE signal is strongly suppressed between magnetic field values of between around ±520 Oe at 175 K in the 12 nm flake, serving as clear evidence of the emergent A-type AFM state. (f) The switching fields measured at different temperatures from the 9 nm-thick flake with only the ferromagnetic state and the 12 nm-thick flake with coexisting antiferromagnetic−ferromagnetic states.

https://doi.org/10.1021/acsnano.4c08700
ACS Nano 2024, 18, 33381−33389

Further magnetic characterizations were carried out by a superconducting quantum interference device (SQIUD) using samples transferred on a SiO_2/Si substrate to avoid the strong diamagnetic background signal from mica substrates. The experimental measurements were conducted in both parallel (H//c) and perpendicular (H⊥c) magnetic fields, as illustrated in Figure 2a,c. Initially, the sample underwent a cooling process under out-of-plane magnetic fields of 1000 Oe (FC) as well as at zero field (ZFC). The behavior of the averaged magnetic moment with temperature revealed the presence of intrinsic ferromagnetism in our CVD-grown Cr_5Te_8 samples. Below 190 K (T_c), a net magnetic moment emerged, gradually reaching a maximum as the temperature decreased further. Notably, at 25 K (freezing temperature T_f), the ZFC curve exhibited a decline in magnetic susceptibility, showing a spin-glass-like behavior. The manifestation of such a spin-glass-like behavior is common in certain spin-frustrated systems like $Cr_7(Se_{1-x}Te_x)_8$ compounds,[29] where a competition between AFM and FM interactions exists. Further investigation is needed to clarify this phenomenon such as using AC magnetization measurements to probe potential glassy behavior. Moreover, the maximum magnetic moment under an out-of-plane magnetic field reached 160 μemu, surpassing that under an in-plane field, indicating an out-of-plane anisotropy for ferromagnetism. The magnetic field-dependent susceptibility curves (probing hysteresis loops) depicted in Figure 2b were obtained at various temperatures ranging from 250 to 1.8 K under an out-of-plane magnetic field. At 1.8 K, the remnant magnetization, saturated magnetization, and coercive fields were measured at 210 μemu, 212 μemu, and 7164 Oe, respectively. Even at 220 K under in-plane magnetic fields (Figure 2d), a hysteresis loop is still observable, suggesting that the T_c of our sample extends to 220 K.

To further determine the magnetic order in individual Cr_5Te_8 flakes, we performed a polar magneto-optical Kerr effect (MOKE) measurement with the perpendicular magnetic field in the Faraday configuration (Figure 3a). A 635 nm linearly polarized laser beam with normal incidence and an estimated power of 3 μW on the sample was employed to carry out the MOKE measurements. The split beams after passing through a chopper and a Wollaston prism were collected by two photodiodes in a differential mode whose output results were received by a current preamplifier. The measured normalized signals can detect Kerr rotations (rotation of the polarization angle), θ_K, after a conversion factor. Since tellurides are sensitive to air and easy to degrade, particularly for ultrathin flakes with thicknesses below 10 nm, PMMA was spin-coated to protect Cr_5Te_8 before the MOKE measurement. Figure 3b shows the MOKE signal from a 12 nm flake of Cr_5Te_8 at 5 K (Figure S3a). The observed hysteresis curves, coupled with the magnetization at zero magnetic field, are distinctive indicators of FM ordering. Figure 3c displays the temperature dependence of the hysteresis curves in the MOKE signal for a 9 nm sample (Figure S3b) from 160 to 230 K. The rising point of the curve measured when the magnetic field was swept from negative to positive is taken as the switching field. We observed that the switching field gradually decreases with increasing temperature for the 9 nm sample (Figure 3c,f). We defined T_c as the midpoint between the two temperatures at which the switching fields are about to disappear and disappear completely. A high T_c of 225 K was obtained in the 9 nm sample, which is competitive compared with the values of 210 and 200 K for Fe_3GeTe_2[6] and other Cr_5Te_8 samples in previous reports,[19−21] respectively.

Interestingly, we note the presence of an emergent AFM state in the temperature-dependent MOKE signals of a 12 nm Cr_5Te_8 flake (Figure 3d). When the temperature is lower than 150 K, the signal shows a standard rectangular shape, indicating a state with FM order. However, when the temperature approaches 160−175 K, the hysteresis loops exhibit multiple magnetic states. At 175 K, The MOKE signal is strongly suppressed, with the θ_K approaching zero, for magnetic fields between around ±520 Oe. Upon increasing the magnetic field amplitudes beyond these critical values, θ_K shows a sharp jump to finite values. The suppression of the Kerr signal at zero magnetic field demonstrates that the ground state of the system has zero out-of-plane magnetization. This is consistent with an emergent A-type AFM interlayer coupling,[17,30] suggesting that within one slab of $CrTe_2$, all spin moments are aligned ferromagnetically, but across the van der Waals gap, these moments are coupled antiferromagnetically.[22] Based on the MOKE signal at 175 K, we can assign the magnetic order in these three states (Figure 3e) by assuming an A-type AFM interlayer coupling. At the intermediate state 2 under a magnetic field between ±520 Oe, the magnetization of the two slabs of the $CrTe_2$ system is oppositely oriented, causing the net magnetization to vanish and the system to behave as an antiferromagnet with an exchange field of about 520 Oe. For states 1 and 3, when the absolute value of the applied magnetic field exceeds 520 Oe, the magnetization of one of the slabs that was previously antiparallel with the field flips sharply to align with the external magnetic field, restoring the out-of-plane magnetization with a magnetic field-driven transition from AFM ordering to a fully spin-polarized state.

This outcome indicates that introducing Cr atoms into the vdW gaps of $CrTe_2$ triggers a shift in the magnetic behavior from FM to AFM states by modifying the interlayer magnetic interactions. The mechanism of the emergence of an AFM exchange coupling in 2D Cr_5Te_8 remains an open question. It is noteworthy that similar magnetic transitions from AFM to FM states in Cr_5Te_8[22] and upon Co doping in Fe_4GeTe_2[31] have been documented and attributed to changes in Ruderman−Kittel−Kasuya−Yosida (RKKY) interaction dynamics. The RKKY model suggests that the interlayer magnetic coupling energy in synthetic AFM multilayers fluctuates as a function of the nonmagnetic layer thickness. This leads to the hypothesis that RKKY interactions can be modified with a minor reduction in the lattice parameter along the c-axis in Cr_5Te_8 and Co doped Fe_4GeTe_2, which can be affected by temperature changes. For bulk Cr_5Te_8, only in the temperature range of 150−180 K does AFM interlayer coupling between the adjacent $CrTe_2$ layers show up.[22] The striking similarities to our observations suggest that RKKY coupling is involved in our observation of emergent AFM ordering. So in our case, the intercalated Cr atoms can reduce the lattice constant along the c-axis relative to that of nonintercalated $CrTe_2$, suggesting an increase of the coupling along the c-axis direction.[22] This change in the lattice constant along the c-axis can modulate the strength and sign of the RKKY interaction, potentially favoring a coexistence of FM and AFM ordering within this specific temperature range between 160 and 180 K.

In addition, as the temperature rises, the switching fields of the 12 nm flake initially increase and then decrease (blue curve), distinct from the 9 nm flake with a monotonic linear decrease in the switching field (orange curve), as depicted in

https://doi.org/10.1021/acsnano.4c08700
ACS Nano 2024, 18, 33381−33389

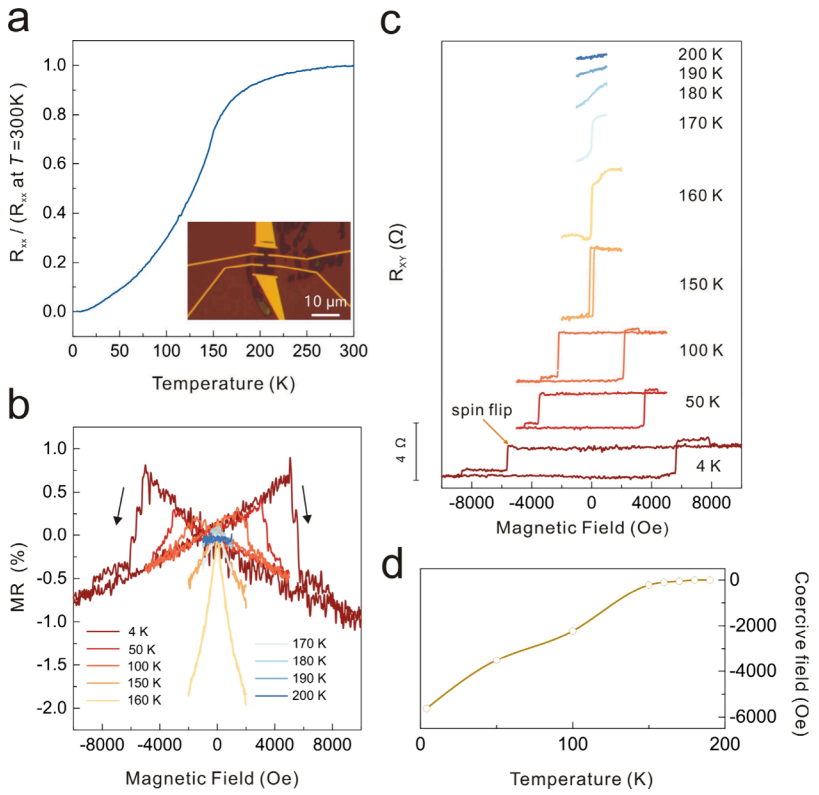

Figure 4. Transport measurements of a 12 nm-thick Cr_5Te_8 Hall device. (a) Temperature dependence of the longitudinal resistance R_{xx} normalized by the value at 300 K measured at zero magnetic field. Inset: corresponding optical microscopy image of the Hall device. Scale bar, 10 μm. (b) Magnetoresistance (MR) and (c) R_{xy} versus out-of-plane magnetic field at different temperatures for the device. Black arrows in (b) label the sweep directions of magnetic field for the 4 K MR curves. The orange arrow in (c) shows the spin-flip transition for subtracting coercive field. (d) Temperature dependence of the extracted negative coercive fields (yellow) from R_{xy} hysteresis loops.

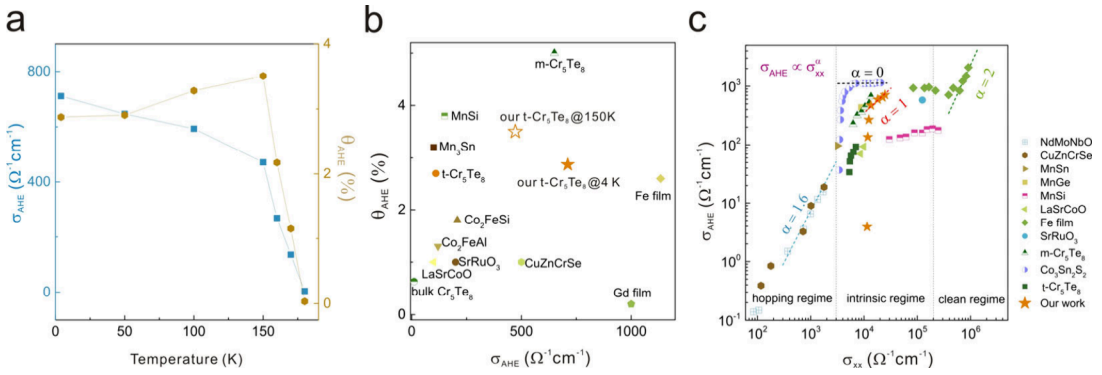

Figure 5. Anomalous Hall effects (AHEs) for 2D Cr_5Te_8 and other metallic ferromagnets. (a) Temperature dependence of the σ_{AHE} and θ_{AHE} at zero magnetic field of the 2D Cr_5Te_8 Hall device studied in Figure 4. (b) Comparison of the σ_{AHE} and θ_{AHE} of our 2D Cr_5Te_8 with those of other metallic ferromagnetic materials. The 2D Cr_5Te_8 exhibits exceptional AHE performance, with a σ_{AHE} of 710 Ω^{-1} cm^{-1} and a θ_{AHE} of 3.5%, surpassing most other metallic ferromagnets. (c) σ_{AHE} versus σ_{xx} for 2D Cr_5Te_8 and other ferromagnets on a log−log graph spanning the various AHE regimes.

Figure 3f. This phenomenon suggests that the AFM state has a relatively weak interlayer exchange coupling, allowing a switching between the interlayer AFM and FM states by tuning the temperature. For the AFM−FM coexistence in the 12 nm flake and its absence in the 9 nm flake, we hypothesize that this behavior is related to the interlayer exchange coupling and RKKY interactions. In the 12 nm flake, the balance between these interactions may favor the stabilization of an AFM state at certain temperatures, while the FM state dominates in thinner flakes due to stronger surface effects that stabilize the FM state.

We further proceeded to fabricate Hall devices (shown in Figure 4a, inset, and Figure S4) and carried out magnetotransport investigations to analyze the out-of-plane magnetic anisotropy. The temperature-dependent longitudinal resistance (R_{xx}) of another 12 nm-thick Cr_5Te_8 flake, normalized by its value at 300 K, reveals a decrease as the temperature decreases from 300 to 4 K, indicating metallic behavior (Figure 4a). Magnetoresistance (MR) measurements display negative MR under a magnetic field of 1T with distinctive butterfly shaped loops (Figure 4b), transitioning at spin-flip magnetic fields. Negative MR is a common characteristic of FM metals, where

https://doi.org/10.1021/acsnano.4c08700
ACS Nano 2024, 18, 33381−33389

an external magnetic field aligns spins, reduces spin disorder, and minimizes spin-dependent carrier scattering, consequently reducing resistance.[32,33] Interestingly, the largest MR value of 2% is observed at 160 K, surpassing that at 4 K. This unusual temperature dependence of MR is likely linked to the AFM domains, particularly around T_c. The spin filter effect resulting from AFM coupling is expected to amplify the negative MR.[22] Other than that, the Hall resistances (R_{xy}) exhibit a distinct anomalous Hall effect (AHE) with square-shaped hysteresis loops that diminish with rising temperature (as shown in Figure 4c). The persistence of AHE at 170 K indicates that the T_c is at least 170 K in this flake. AHE measurements reveal a consistent trend in the switching field that steadily decreases in amplitude from −5623 Oe at 4 K to almost 0 Oe at 180 K, as depicted in Figure 4d.

We subtract the AHE by removing the ordinary Hall effect (OHE) background from the Hall resistance data. To accurately determine the anomalous Hall conductivity (σ_{AHE}), the OHE background is subtracted to obtain ρ_{xy}^{AHE}, and subsequently, the σ_{AHE} is first calculated by inverting the resistivity matrix [$\sigma_{AHE} = -(\rho_{xy}^{AHE})^2/(\rho_{xx}^2 + (\rho_{xy}^{AHE})^2)$], where ρ_{xy}^{AHE} is the anomalous Hall resistivity and ρ_{xx} is the longitudinal resistivity.[34−38] By combining longitudinal and Hall measurement data, we calculated σ_{AHE} and plotted its temperature dependence (Figure 5a). Starting with a small value of around 4 Ω^{-1} cm^{-1} at 180 K, σ_{AHE} rapidly increases with a steeper slope, reaching a value of around 470 Ω^{-1} cm^{-1} at 150 K as the temperature decreases. From 150 K onward, the slope becomes more gradual as σ_{AHE} continues to increase, ultimately reaching a maximum value of 710 Ω^{-1} cm^{-1} at 4 K. In addition, our Cr_5Te_8 exhibits a large anomalous Hall angle (θ_{AHE}), determined by the ratio of the σ_{AHE} to the longitudinal conductivity (σ_{xx}). As shown in Figure 5a, θ_{AHE} starts at 2.87% at 4 K and then increases with rising temperature, reaching a maximum of approximately 3.5% at around 150 K, before decreasing again as the temperature increases above T_c. Notably, our 2D Cr_5Te_8 exhibits superior AHE performance,[18,21,34−38] achieving a θ_{AHE} of 3.5% (∼150 K) and a large σ_{AHE} of 710 Ω^{-1} cm^{-1} (∼4 K) (Figure 5b), which is three magnitudes larger in σ_{AHE} compared to the bulk Cr_5Te_8 crystal.[18]

To compare the AHE observed in Cr_5Te_8 with other materials,[21,34−42] Figure 5c presents a log−log plot of σ_{AHE} versus σ_{xx} for various materials across different AHE regimes. The map includes different scaling relationships ($\sigma_{AHE} \propto \sigma_{xx}^{\alpha}$) for the localized hopping regime, intrinsic regime, and clean regime. The distinct scaling relationships reflect the underlying mechanisms governing the AHE, such as the interplay between localization, skew scattering, and other intrinsic contributions, which can vary depending on the material and the specific transport regime.[41,42] In the dirty localized hopping regime, the AHE is suppressed by disorder due to the influence of finite-lifetime disorder broadening, such as in $Cu_{1-x}Zn_xCr_2Se_4$ and $La_{1-x}Sr_xCoO_3$, which is well described experimentally by the scaling relation with $\alpha = 1.6$.[37] In the intrinsic regime, $\alpha = 0$ is observed in $Co_3Sn_2S_2$,[35] which is primarily driven by the intrinsic Berry-curvature mechanism in momentum space. In these topological materials, there exists a physical limitation where the σ_{AHE} of the intrinsic Berry-curvature mechanism remains constant. Consequently, as θ_{AHE} increases, σ_{xx} must decrease since $\sigma_{AHE} = \theta_{AHE}\sigma_{xx}$ = constant. In bulk materials like Fe film, this paradox seems to be resolved by having a sample thickness (>1 mm) significantly larger than the typical spin diffusion length of tens of nanometers, which limits further advancements in spin current generation within such bulk materials.[37]

Figure 5c exhibits a clear linear relationship between σ_{AHE} and σ_{xx} in our Cr_5Te_8, representing $\alpha = 1$ scaling below 150 K. Conventionally, $\alpha = 1$ is associated with extrinsic skew-type electron scattering, which is understood as asymmetric scattering for electrons with up and down spin orientations.[43,44] This result can be explained by the Giovannini−Kondo (GK) model with linear scaling ($\alpha = 1$). The crucial ingredient of the GK model is the coupling between the total angular momentum of localized magnetic moments and the orbital motion of mobile electrons, which leads to AHE as the result of the skew scattering.[43] The linear relationship observed in trigonal Cr_5Te_8 suggests that the extrinsic skew-scattering mechanism could be a primary contributor to the AHE in our Cr_5Te_8, rather than the intrinsic Berry-curvature ($\alpha = 0$) or side-jump ($\alpha = 2$) mechanisms. Overall, the potential for large θ_{AHE} and σ_{AHE} suggests exciting prospects for future research into materials exhibiting such AHE behaviors.

CONCLUSION

To summarize, we realized the CVD growth of submillimeter-scale 2D self-intercalated Cr_5Te_8 flakes via vdW epitaxy. The grown Cr_5Te_8 flakes exhibit strong anisotropic FM order, and a T_c above 220 K can be retained down to atomic thickness (9 nm). Additionally, an emergent AFM state is observed in the MOKE signal from ultrathin Cr_5Te_8 flakes in a temperature window of 160−180 K. The AFM state has a relatively weak interlayer exchange coupling, allowing a switching between the interlayer AFM and FM states by tuning the temperature. Notably, through magnetotransport measurements, we unveil the exceptional AHE properties with a giant anomalous Hall conductivity of 710 Ω^{-1} cm^{-1} and an anomalous Hall angle of 3.5%, which surpass those of typical itinerant ferromagnets. Further analysis suggests that the anomalous Hall effect in trigonal Cr_5Te_8 is primarily driven by the skew-scattering mechanism, rather than the intrinsic or extrinsic side-jump mechanism. Our research will contribute greatly to the controlled CVD synthesis of 2D magnetic materials and thereby outline a route toward constructing next-generation low-dissipation electronic and spintronic devices.

METHODS

Growth and Transfer of Cr_5Te_8 Flakes. The growth of the chromium telluride crystals is performed in a three-temperature zone furnace at ambient pressure. The tellurium powder (Alfa Aesar, purity 99.9%) is placed in the first hot zone with the temperature at 500 °C. The mica substrate is put 0.5 cm above the mixture of chromium powder (Alfa Aesar, purity 99.9%), and the sodium chloride powder (Alfa Aesar, purity 99.9%) is placed in the second temperature zone. A mixture of argon and helium in a ratio of 100:15 with a flow rate of 100 sccm is used as the carrier gas to deliver the vapor species to the downstream substrate. The growth temperature is about 800 °C, and the growth time is 10−30 min. As a result, ultrathin chromium telluride flakes are obtained on the mica substrate.

The grown chromium telluride flakes can easily transferred to arbitrary substrates. Chromium telluride flakes on mica are first spin-coated with polystyrene (PS; 50 mg/mL toluene solution) via a spin coater and baked at 60 °C for 10 min. After cooling, polypropylene carbonate (PPC) is spin-coated on the PS/Cr_5Te_8/mica and baked at 110 °C for 10 min. After that, the supporting film with Cr_5Te_8 flakes is torn from mica using tweezers and transferred to a target substrate (e.g., TEM grid or SiO_2/Si) and baked on a heat plate. Finally, that

https://doi.org/10.1021/acsnano.4c08700
ACS Nano 2024, 18, 33381−33389

supporting film is removed by dissolution in acetone for about 30 min and blow-dried under N_2 gas.

Characterizations. An NT-MDT NTEGRA Prima multifunctional atomic force microscope in tapping mode was employed to determine the thickness. HR-STEM as well as EDS mapping were performed with a Thermo Scientific Themis Z instrument at a 300 kV acceleration voltage.

Device Fabrication. Thin flakes were transferred on top of standard doped Si substrates with 285 nm SiO_2. Then the sample was transferred immediately into a high-vacuum e-beam evaporator, and a 1.5 nm-thick Al film (that naturally oxidized into a protective AlO_x layer) was deposited under a pressure of 2.0×10^{-8} Torr to protect the sample surface from oxidation. The electrical contacts (Ti/Pd, 5/35 nm) to chromium telluride flakes were patterned by e-beam lithography. Before the contacts were deposited, the exposed areas were etched by reactive ion etching (RIE) in a Panasonic E620 ICP system with BCl_3 + Ar plasma to remove the thin layer of AlO_x so that ohmic contacts could be achieved. A physical property measurement system (Quantum Design) at a magnetic field of up to 9 T and at temperatures from 300 to 2 K was employed to measure the transport properties. The Hall resistance traces dependent on the magnetic field were antisymmetrized to eliminate field-even characteristics from the Hall effect traces. These features arise from the mixing of R_{xx} with R_{xy} due to device geometry and electrode misalignment.

ASSOCIATED CONTENT

Supporting Information

The Supporting Information is available free of charge at https://pubs.acs.org/doi/10.1021/acsnano.4c08700.

Schematic of Cr_5Te_8 growth process, EDS elemental mapping of Cr−L and Te−L, and atomic force microscopy topographic images of Cr_5Te_8 flakes in MOKE and magnetotransport measurements (PDF)

AUTHOR INFORMATION

Corresponding Authors

Lei Fu − *Department of Physics and Astronomy, Birck Nanotechnology Center, and Purdue Quantum Science and Engineering Institute, Purdue University, West Lafayette, Indiana 47907, United States;* orcid.org/0000-0001-7638-3077; Email: fu302@purdue.edu, hileifu@gmail.com

Yong P. Chen − *Department of Physics and Astronomy, Birck Nanotechnology Center, and Purdue Quantum Science and Engineering Institute, Purdue University, West Lafayette, Indiana 47907, United States; School of Electrical and Computer Engineering, Purdue University, West Lafayette, Indiana 47907, United States; Institute of Physics and Astronomy and Villum Centers for Dirac Materials and for Hybrid Quantum Materials, Aarhus University, 8000 Aarhus-C, Denmark; WPI Advanced Institute for Materials Research (AIMR), Tohoku University, Sendai 980-8577, Japan*; Email: yongchen@purdue.edu

Author

A. E. Llacsahuanga Allcca − *Department of Physics and Astronomy, Birck Nanotechnology Center, and Purdue Quantum Science and Engineering Institute, Purdue University, West Lafayette, Indiana 47907, United States;* orcid.org/0000-0003-0414-5613

Complete contact information is available at: https://pubs.acs.org/10.1021/acsnano.4c08700

Notes

The authors declare no competing financial interest.

ACKNOWLEDGMENTS

This work was supported in part by the U.S. Department of Energy (DOE) Office of Science through the Quantum Science Center (QSC, a National Quantum Information Science Research Center) and Department of Defense (DOD) Multidisciplinary University Research Initiatives (MURI) program (FA9550-20-1-0322) for materials and device fabrication and MOKE and STEM measurements. We thank Prof. Hongjun Gao for the support and helpful discussions during the earlier stage of the work. We also thank John F. Ribeiro for experiment help in the transport measurements.

REFERENCES

(1) Wang, Q. H.; Kalantar-Zadeh, K.; Kis, A.; Coleman, J. N.; Strano, M. S. Electronics and Optoelectronics of Two-Dimensional Transition Metal Dichalcogenides. *Nat. Nanotechnol.* **2012**, *7*, 699−712.

(2) Mak, K. F.; Shan, J. Photonics and Optoelectronics of 2D Semiconductor Transition Metal Dichalcogenides. *Nat. Photonics* **2016**, *10*, 216−226.

(3) Lee, C. H.; Lee, G. H.; van der Zande, A. M.; Chen, W. C.; Li, Y. L.; Han, M. Y.; Cui, X.; Arefe, G.; Nuckolls, C.; Heinz, T. F.; Guo, J.; Hone, J.; Kim, P. Atomically Thin P−N Junctions with van der Waals Heterointerfaces. *Nat. Nanotechnol.* **2014**, *9*, 676−681.

(4) Wang, H.; Huang, X.; Lin, J.; Cui, J.; Chen, Y.; Zhu, C.; Liu, F.; Zeng, Q.; Zhou, J.; Yu, P.; Wang, X.; He, H.; Tsang, S. H.; Gao, W.; Suenaga, K.; Ma, F.; Yang, C.; Lu, L.; Yu, T.; Teo, E. H. T.; Liu, G.; Liu, Z. High−Quality Monolayer Superconductor $NbSe_2$ Grown by Chemical Vapour Deposition. *Nat. Commun.* **2017**, *8*, 394.

(5) Fei, Z.; Zhao, W.; Palomaki, T. A.; Sun, B.; Miller, M. K.; Zhao, Z.; Yan, J.; Xu, X.; Cobden, D. H. Ferroelectric Switching of a Two−Dimensional Metal. *Nature* **2018**, *560*, 336−339.

(6) Huang, B.; Clark, G.; Navarro-Moratalla, E.; Klein, D. R.; Cheng, R.; Seyler, K. L.; Zhong, D.; Schmidgall, E.; McGuire, M. A.; Cobden, D. H.; Yao, W.; Xiao, D.; Jarillo-Herrero, P.; Xu, X. Layer-Dependent Ferromagnetism in a Van der Waals Crystal Down to the Monolayer Limit. *Nature* **2017**, *546*, 270−273.

(7) Akinwande, D.; Petrone, N.; Hone, J. Two−Dimensional Flexible Nanoelectronics. *Nat. Commun.* **2014**, *5*, 5678.

(8) Myny, K. The Development of Flexible Integrated Circuits Based on Thin−Film Transistors. *Nat. Electron.* **2018**, *1*, 30−39.

(9) Fei, Z.; Huang, B.; Malinowski, P.; Wang, W.; Song, T.; Sanchez, J.; Yao, W.; Xiao, D.; Zhu, X.; May, A. F.; Wu, W.; Cobden, D. H.; Chu, J. H.; Xu, X. Two−Dimensional Itinerant Ferromagnetism in Atomically Thin Fe_3GeTe_2. *Nat. Mater.* **2018**, *17*, 778−782.

(10) Kim, K.; Seo, J.; Lee, E.; Ko, K.-T.; Kim, B. S.; Jang, B. G.; Ok, J. M.; Lee, J.; Jo, Y. J.; Kang, W.; Shim, J. H.; Kim, C.; Yeom, H. W.; Il Min, B.; Yang, B.-J.; Kim, J. S. Large Anomalous Hall Current Induced by Topological Nodal Lines in a Ferromagnetic van der Waals Semimetal. *Nat. Mater.* **2018**, *17*, 794−799.

(11) Deng, Y. J.; Yu, Y. J.; Song, Y. C.; Zhang, J. Z.; Wang, N. Z.; Sun, Z. Y.; Yi, Y. F.; Wu, Y. Z.; Wu, S. W.; Zhu, J. Y.; Wang, J.; Chen, X. H.; Zhang, Y. B. Gate−Tunable Room−Temperature Ferromagnetism in Two−Dimensional Fe_3GeTe_2. *Nature* **2018**, *563*, 94−99.

(12) Zheng, G.; Xie, W. Q.; Albarakati, S.; Algarni, M.; Tan, C.; Wang, Y.; Peng, J.; Partridge, J.; Farrar, L.; Yi, J.; Xiong, Y.; Tian, M.; Zhao, Y. J.; Wang, L. Gate-Tuned Interlayer Coupling in Van Der Waals Ferromagnet Fe_3GeTe_2 Nanoflakes. *Phys. Rev. Lett.* **2020**, *125*, No. 047202.

(13) Bonilla, M.; Kolekar, S.; Ma, Y. J.; Diaz, H. C.; Kalappattil, V.; Das, R.; Eggers, T.; Gutierrez, H. R.; Phan, M. H.; Batzill, M. Strong Room−Temperature Ferromagnetism in VSe_2 Monolayers on van der Waals Substrates. *Nat. Nanotechnol.* **2018**, *13*, 289−293.

(14) Meng, L.; Zhou, Z.; Xu, M.; Yang, S.; Si, K.; Liu, L.; Wang, X.; Jiang, H.; Li, B.; Qin, P.; Zhang, P.; Wang, J.; Liu, Z.; Tang, P.; Ye, Y.; Zhou, W.; Bao, L.; Gao, H.−J.; Gong, Y. Anomalous Thickness

Dependence of Curie Temperature in Air−Stable Two−Dimensional Ferromagnetic 1T−$CrTe_2$ Grown by Chemical Vapor Deposition. *Nat. Commun.* **2021**, *12*, 809.
(15) Wen, Y.; Liu, Z.; Zhang, Y.; Xia, C.; Zhai, B.; Zhang, X.; Zhai, G.; Shen, C.; He, P.; Cheng, R.; Yin, L.; Yao, Y.; Getaye Sendeku, M.; Wang, Z.; Ye, X.; Liu, C.; Jiang, C.; Shan, C.; Long, Y.; He, J. Tunable Room−Temperature Ferromagnetism in Two−Dimensional Cr_2Te_3. *Nano Lett.* **2020**, *20*, 3130−3139.
(16) Gong, C.; Li, L.; Li, Z. L.; Ji, H. W.; Stern, A.; Xia, Y.; Cao, T.; Bao, W.; Wang, C. Z.; Wang, Y. A.; Qiu, Z. Q.; Cava, R. J.; Louie, S. G.; Xia, J.; Zhang, X. Discovery of Intrinsic Ferromagnetism in Two−Dimensional van der Waals Crystals. *Nature* **2017**, *546*, 265−269.
(17) Cheng, G.; Rahman, M. M.; Allcca, A. L.; Rustagi, A.; Liu, X.; Liu, L.; Fu, L.; Zhu, Y.; Mao, Z.; Watanabe, K.; Taniguchi, T.; Upadhyaya, P.; Chen, Y. P. Electrically Tunable Moiré Magnetism in Twisted Double Bilayers of Chromium Triiodide. *Nat. Electron.* **2023**, *6*, 434−442.
(18) Wang, Y.; Yan, J.; Li, J.; Wang, S.; Song, M.; Song, J.; Li, Z.; Chen, K.; Qi, Y. Magnetic Anisotropy and Topological Hall Effect in the Trigonal Chromium Tellurides Cr_5Te_8. *Phys. Rev. B* **2019**, *100*, 022434.
(19) Wu, H. X.; Guo, J. F.; Zhaxi, S.; Xu, H.; Mi, S.; Wang, L.; Chen, S. S.; Xu, R.; Ji, W.; Pang, F.; Cheng, Z. H. Controllable CVD Growth of 2d Cr_5Te_8 Nanosheets with Thickness-Dependent Magnetic Domains. *ACS Appl. Mater. & Interfaces* **2023**, *15*, 26148−26158.
(20) Chen, C.; Chen, X.; Wu, C.; Wang, X.; Ping, Y.; Wei, X.; Zhou, X.; Lu, J.; Zhu, L.; Zhou, J.; Zhai, T.; Han, J.; Xu, H. Air-Stable 2d Cr_5Te_8 Nanosheets with Thickness-Tunable Ferromagnetism. *Adv. Mater.* **2021**, *34* (2), 2107512.
(21) Tang, B. J.; Wang, X. W.; Han, M. J.; Xu, X. D.; Zhang, Z. W.; Zhu, C.; Cao, X.; Yang, Y. M.; Fu, Q. D.; Yang, J. Q.; Li, X. J.; Gao, W. B.; Zhou, J. D.; Lin, J. H.; Liu, Z. Phase Engineering of Cr_5Te_8 with Colossal Anomalous Hall Effect. *Nat. Electron.* **2022**, *5*, 224−232.
(22) Zhang, X.; Liu, W.; Niu, W.; Lu, Q.; Wang, W.; Sarikhani, A.; Wu, X.; Zhu, C.; Sun, J.; Vaninger, M.; Miceli, P. F.; Li, J.; Singh, D. J.; Hor, Y. S.; Zhao, Y.; Liu, C.; He, L.; Zhang, R.; Bian, G.; Yu, D.; Xu, Y. Self-Intercalation Tunable Interlayer Exchange Coupling in a Synthetic Van Der Waals Antiferromagnet. *Adv. Funct. Mater.* **2022**, *32*, No. 2202977.
(23) Yang, J.; Wang, X.; Li, S.; Wang, X.; Pan, M.; Ai, M.; Yuan, H.; Peng, X.; Wang, R.; Li, Q.; Zheng, F.; Zhang, P. Robust Two-Dimensional Ferromagnetism in $Cr_5Te_8/CrTe_2$ Heterostructure with Curie Temperature above 400 K. *ACS Nano* **2023**, *17*, 23160−23168.
(24) Dijkstra, J.; Weitering, H. H.; Bruggen, C. F. v.; Haas, C.; Groot, R. A. d. Band-Structure Calculations, and Magnetic and Transport Properties of Ferromagnetic Chromium Tellurides (CrTe, Cr_3Te_4, Cr_2Te_3). *J. Phys.: Condens. Matter* **1989**, *1*, 9141−9161.
(25) Hamasaki, T.; Hashimoto, T.; Yamaguchi, Y.; Watanabe, H. Neutron−Diffraction Study of Cr_2Te_3 Single−Crystal. *Solid State Commun.* **1975**, *16*, 895−897.
(26) Hashimoto, T.; Hoya, K.; Yamaguchi, M.; Ichitsubo, I. Magnetic Properties of Single Crystals $Cr_{2-\delta}Te_3$. *J. Phys. Soc. Jpn.* **1971**, *31*, 679−685.
(27) Andresen, A. F.; Zeppezauer, E.; Boive, T.; Nordstrom, B.; Brändén, C.-I. The Magnetic Structure of Cr_2Te_3, Cr_3Te_4, and Cr_5Te_6. *Acta Chem. Scand.* **1970**, *24*, 3495.
(28) Zhou, J.; Lin, J.; Huang, X.; Zhou, Y.; Chen, Y.; Xia, J.; Wang, H.; Xie, Y.; Yu, H.; Lei, J.; Wu, D.; Liu, F.; Fu, Q.; Zeng, Q.; Hsu, C. H.; Yang, C.; Lu, L.; Yu, T.; Shen, Z.; Lin, H.; Yakobson, B. I.; Liu, Q.; Suenaga, K.; Liu, G.; Liu, Z. A Library of Atomically Thin Metal Chalcogenides. *Nature* **2018**, *556*, 355−359.
(29) Li, Y. B.; Zhang, Y. Q.; Li, W. F.; Li, D.; Li, J.; Zhang, Z. D. Spin−Glass−Like Behavior and Electrical Transport Properties of $Cr_7(Se_{1-x}Te_x)_8$. *Phys. Rev. B* **2006**, *73*, No. 212403.
(30) Jiang, S. W.; Li, L. Z.; Wang, Z. F.; Mak, K. F.; Shan, J. Controlling Magnetism in 2d CrI_3 by Electrostatic Doping. *Nat. Nanotechnol.* **2018**, *13*, 549−553.
(31) Wang, M.; Zhu, K.; Lei, B.; Deng, Y.; Hu, T.; Song, D.; Du, H.; Tian, M.; Xiang, Z.; Wu, T.; Chen, X. Layer-Number-Dependent Magnetism in the Co-Doped Van Der Waals Ferromagnet Fe_3GaTe_2. *Nano Lett.* **2024**, *24* (14), 4141.
(32) von Helmolt, R.; Wecker, J.; Holzapfel, B.; Schultz, L.; Samwer, K. Giant Negative Magnetoresistance in Perovskitelike $La_{2/3}Ba_{1/3}MnO_x$ Ferromagnetic Films. *Phys. Rev. Lett.* **1993**, *71*, 2331−2333.
(33) Yamada, H.; Takada, S. Negative Magnetoresistance of Ferromagnetic Metals Due To Spin Fluctuations. *Prog. Theor. Phys.* **1972**, *48*, 1828−1848.
(34) Asamitsu, A.; Miyasato, T.; Ab, N.; Fujii, T.; Onose, S.; Onoda, S.; Nagaosa, N.; Tokura, Y. Anomalous Hall Effect and Nernst Effect in Itinerant Ferromagnets. *J. Magn. Magn. Mater.* **2007**, *310*, 2000−2002.
(35) Liu, E.; Sun, Y.; Kumar, N.; Muechler, L.; Sun, A.; Jiao, L.; Yang, S.-Y.; Liu, D.; Liang, A.; Xu, Q.; Kroder, J.; Süß, V.; Borrmann, H.; Shekhar, C.; Wang, Z.; Xi, C.; Wang, W.; Schnelle, W.; Wirth, S.; Chen, Y.; Goennenwein, S. T. B.; Felser, C. Giant Anomalous Hall Effect in a Ferromagnetic Kagome-Lattice Semimetal. *Nat. Phys.* **2018**, *14*, 1125−1131.
(36) Manyala, N.; Sidis, Y.; DiTusa, J. F.; Aeppli, G.; Young, D. P.; Fisk, Z. Large Anomalous Hall Effect in a Silicon-Based Magnetic Semiconductor. *Nat. Mater.* **2004**, *3*, 255−262.
(37) Miyasato, T.; Abe, N.; Fujii, T.; Asamitsu, A.; Onoda, S.; Onose, Y.; Nagaosa, N.; Tokura, Y. Crossover Behavior of the Anomalous Hall Effect and Anomalous Nernst Effect in Itinerant Ferromagnets. *Phys. Rev. Lett.* **2007**, *99*, No. 086602.
(38) Nakatsuji, S.; Kiyohara, N.; Higo, T. Large Anomalous Hall Effect in a Non-Collinear Antiferromagnet at Room Temperature. *Nature* **2015**, *527*, 212−215.
(39) Tian, Y.; Ye, L.; Jin, X. F. Proper Scaling of the Anomalous Hall Effect. *Phys. Rev. Lett.* **2009**, *103*, No. 087206.
(40) Ye, L.; Tian, Y.; Jin, X. F.; Xiao, D. Temperature Dependence of the Intrinsic Anomalous Hall Effect in Nickel. *Phys. Rev. B* **2012**, *85*, No. 220403.
(41) Iguchi, S.; Hanasaki, N.; Tokura, Y. Scaling of Anomalous Hall Resistivity in $Nd_2(Mo_{1-x}Nb_x)_2O_7$ with Spin Chirality. *Phys. Rev. Lett.* **2007**, *99*, No. 077202.
(42) Nayak, A. K.; Fischer, J. E.; Sun, Y.; Yan, B. H.; Karel, J.; Komarek, A. C.; Shekhar, C.; Kumar, N.; Schnelle, W.; Kübler, J.; Felser, C.; Parkin, S. S. P. Large Anomalous Hall Effect Driven by a Nonvanishing Berry Curvature in the Noncolinear Antiferromagnet Mn_3Ge. *Sci. Adv.* **2016**, *2*, No. e1501870.
(43) Maryenko, D.; Mishchenko, A. S.; Bahramy, M. S.; Ernst, A.; Falson, J.; Kozuka, Y.; Tsukazaki, A.; Nagaosa, N.; Kawasaki, M. Observation of Anomalous Hall Effect in a Non-Magnetic Two-Dimensional Electron System. *Nat. Commun.* **2017**, *8*, 14777.
(44) Liu, Y.; Petrovic, C. Anomalous Hall Effect in the Trigonal Cr_5Te_8 Single Crystal. *Phys. Rev. B* **2018**, *98*, No. 195122.

https://doi.org/10.1021/acsnano.4c08700
ACS Nano 2024, 18, 33381−33389